Applied Magnetic Resonance
https://doi.org/10.1007/s00723-024-01657-9

Exploring the Triplet State of Chlorophyll *a* in Mesoporous Silica Matrices by Time-Resolved EPR

Samuel Zatta[1] · Andrea Calcinoni[1] · Alessandro Agostini[1] · Silvia Leccese[2] · Thomas Onfroy[2] · Claude Jolivalt[2] · Alberto Mezzetti[2] · Marco Bortolus[1] · Donatella Carbonera[1]

Received: 16 May 2023 / Revised: 17 April 2024 / Accepted: 18 April 2024

Abstract
Chlorophyll is a pivotal molecule in photosynthesis due to its ability to absorb solar light and start the photochemical process. The chlorophyll triplet state is easily populated from the light-induced singlet excited state via Intersystem Crossing (ISC) and can react with oxygen generating singlet oxygen, posing a threat to the stability of chlorophyll, but also an opportunity for photodynamic therapy. Here, we focus on the study of the photo-physical properties of chlorophyll *a* and WSCP (Water-Soluble Chlorophyll Protein, a protein binding the pigment), which have been adsorbed in mesoporous silica matrices. We adopt SBA-15, a silica matrix with well-ordered hexagonal structure with pores of 70 Å of diameter. The triplet formed upon illumination in these systems is studied by time-resolved EPR spectroscopy. Analysis of the EPR spectra shows that the triplet state is very sensitive to the inclusion in the pores of SBA-15 modifying its spin polarization. Chl *a* in SBA-15 loses its central metal ion, while its structure remains unchanged if the mesoporous silica is previously soaked into a basic solution before Chl *a* adsorption, as revealed by its zero-field splitting parameters of the triplet state. WSCP is readily included in the silica matrix, but its embedded pigments are no longer protected by the protein core.

1 Introduction

Chlorophylls, in particular Chlorophyll *a* (Chl *a*, see Fig. 1, left panel), are the main pigments involved in oxygenic photosynthesis, but their importance is not only limited to natural photosynthesis. These pigments and their derivatives can also be exploited in the medical field as new photosensitizers drugs for photodynamic

✉ Marco Bortolus
marco.bortolus@unipd.it

[1] Department of Chemical Sciences, University of Padova, Via Marzolo 1, 35131 Padua, Italy

[2] Laboratoire de Réactivité de Surface, LRS, Sorbonne Université, CNRS, 75005 Paris, France

Published online: 06 May 2024

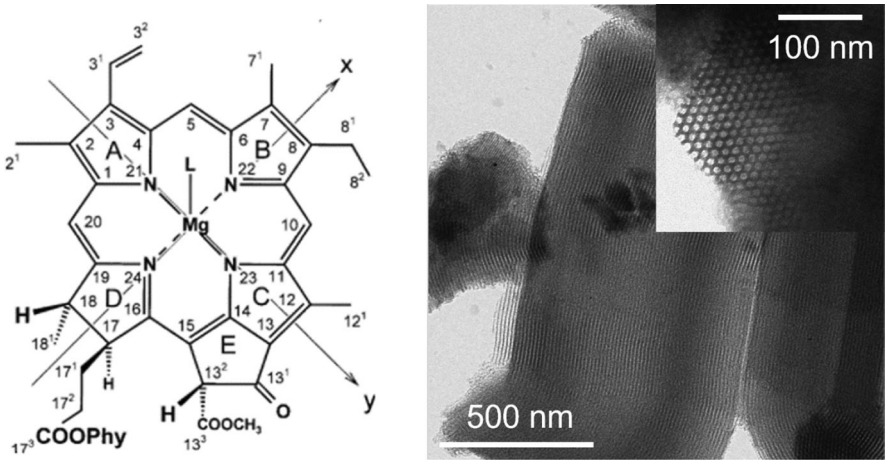

Fig. 1 (Left) Molecular structure of chlorophyll *a* with numbering of rings, according to IUPAC-IUB nomenclature. The two diagonal axes indicate the direction of the two optical polarization axes, *x* and *y*. *Phy* indicates the phytyl side chain. L indicates a potential axial ligand, depending on the coordinating capability of the environment. (Right) Transmission Electron Microscopy image of SBA particles showing the elongated morphology (1500 nm length–750 nm width) and in the inset the hexagonal structure of the pores

therapy (PDT) both in the treatment against microbial infection [1] and in the fight against cancer [2]. They can also be used as catalysts when embedded in various innovative systems for water splitting [3–5], H_2 production and CO_2 conversion [6, 7]. Finally, they are suitable candidates in the development for artificial photosynthesis [8, 9] in the global race to find environmental-friendly alternative energy sources to satisfy the growing worldwide request for energy.

Chlorophylls have an intrinsic high rate of Intersystem Crossing (ISC) and populate excited triplet states with high yield (> 60% in organic solvent) [10]. In turn, chlorophyll triplet states have the right energy to react with oxygen, generating excited singlet oxygen [11, 12]:

$$^3\mathrm{Chl}^* + {}^3\mathrm{O}_2 \rightarrow {}^1\mathrm{Chl} + {}^1\mathrm{O}_2^*$$

Singlet oxygen is a highly reactive and oxidant species with an ambivalent role: it is the main oxidizing agent in PDT, but can damage the chlorophyll itself, leading to photobleaching, and also, in a biological context, other relevant molecules, such as proteins and lipids [12].

Nature, in photosynthetic systems, prevents the damage deactivating the Chl *a* triplet state via triplet–triplet energy transfer, a mechanism in which the triplet excitation transfers from chlorophyll to nearby carotenoid before it can react with oxygen [13–15]. However, since singlet oxygen is a desirable product, overcoming Chl *a* photobleaching while sustaining its production would be ideal for PDT. Nature provides a second example of photoprotection in Water-Soluble Chlorophyll Protein (WSCP), a tetrameric protein storing four chlorophyll molecules arranged in a dimer

of dimers [16]; the hydrophobic protein core hosting the Chlorophylls is accessible from the solution by oxygen and other solutes [17]. Interestingly, WSCP is able to generate singlet oxygen, but at the same time its Chls are highly protected toward photobleaching [18], making it suitable for applications that need a stable source of photosensitized singlet oxygen [19]. Since the protein does not bind carotenoids [16], the photoprotection mechanism has been suggested to rely on the steric shielding of critical carbon atoms of the chlorine ring that are sensitive to oxygen attack [18]; the shielding is afforded by the specific conformation of the phytyls, the long hydrophobic chains connected to the chlorin ring of the chlorophyll, adopted in the WSCP core [20]. It has been proposed that the phytyl can either shield the methine or limit the interaction with the singlet oxygen by lowering the residency time of this species near the macrocycle, however, the exact mechanism of photoprotection remains to be understood [17, 18, 20–22].

Besides photobleaching, the other challenge for the use of Chl *a* in PDT is their insolubility in water. Confinement of Chl *a* in a stable porous matrix could improve both its stability and solubility and improve its technological prospects. In particular, Mesoporous Silica (MS) was developed as delivery media for PDT and proved to be effective [23–25]. Ito et al. [26, 27] have shown that chlorophyll-mesoporous silica conjugates are more stable in aqueous solutions than chlorophyll itself. Rizzi et al. [28] adsorbed Chl *a* in MS and showed that amine derivatization of MCM-41 improves adsorption levels and allows photoactive Chl *a* to be available in aqueous solution. Among mesoporous silica nanoparticles, SBA-15 (Santa Barbara Amorphous), a matrix with well-ordered hexagonal structure (p6mm space group) (Fig. 1, right panel), synthesized for the first time in 1998 through a cooperative self-assembly process [29], was proved to be suitable for different applications [24, 30], i.e., bio-imaging and theranostic applications, due to its biocompatibility, or catalysis, due to its stability in water and in most organic solvents. The pore sizes of SBA-15 matrices (ranging from 5 to 30 nm) make them perfect structures to also host proteins and immobilize them [31, 32]. In addition, Chl *a* has been covalently linked to functionalized SBA-15 derivatives showing similar properties to free Chl *a* [33–35]. In this work, we prepare both Chl *a*/SBA-15 and WSCP/SBA-15 conjugates in light of their use for technological applications in photodynamic therapy, in particular aiming at the characterization of the triplet state of Chl *a* as a diagnostic tool for the chemical state of the pigment and the protein in these preparations. SBA-15, as prepared or treated with a basic solution, are impregnated by Chl *a* or WSCP from solution and then dried, obtaining samples were Chl *a* or WSCP are adsorbed on SBA-15. Using Time-Resolved EPR (TR-EPR), we explore the triplet state of Chl *a* in the dried samples and, for comparison, in frozen solution, both for the naked pigment and when hosted into WSCP. The results are compared with those obtained from UV–VIS spectroscopy on solution samples.

2 Materials and Methods

All chemicals, unless specified, were purchased from Merck (Germany) and used without further purification.

2.1 SBA-15 Preparation

SBA-15 was prepared starting from the method used by Zhao et al. [29], with some modifications, according to the following procedure. SBA-15 was synthesized using a triblock copolymer, Pluronic P123 ($(EO)_{20}(PO)_{70}(EO)_{20}$ from Sigma Aldrich), as a structure directing agent. In a typical synthesis 8.02 g of P123 are mixed under stirring at 750 rpm 280 mL of 0.1 mol/L HCl for 2 h at 40 °C until dissolution of P123 and formation of mesostructured phase of micelles. 16.80 g of tetraethyl-orthosilicate (TEOS; Aldrich; 98%) as silica precursor is added drop by drop to the solution under stirring at around 500 rpm.

Mesostructured silica sol–gel is obtained after stirring the mixture at 40 °C for 24 h. The sol–gel suspension is then hydrothermally treated for 24 h at 120 °C. The solid obtained is filtrated and thoroughly washed with 4 L of distilled water to remove P123 and then is dried at 80 °C overnight and calcined for 6 h at 550 °C with a temperature ramp of 0.4 °C/min under air flow (300 mL/min) to remove the template. Around 4 g of SBA-15 material were obtained.

The morphology of SBA-15 (Fig. 1, right panel) was characterized by Transmission Electron Microscopy (TEM) images were recorded with a JEOL TEM 100 CXII electron microscope operating at an acceleration voltage of 100 kV. Prior observations, the sample powders were deposited on 3 mm copper grid coated with an amorphous carbon film. The samples were prepared by dispersing in pure alcohol using ultrasonic cleaner and putting a drop of this suspension on grid.

The specific surface area, pore size distribution, and total pore volume of SBA-15 used in this project were determined by recording nitrogen adsorption isotherms. As a pretreatment step, SBA-15 was dehydrated at 120 °C overnight under vacuum. Nitrogen adsorption isotherms at 77 K were measured on BELSORP max apparatus. The specific surface area was obtained using the Brunauer–Emmett–Teller equation from adsorption values at six relative pressures (P/P_0) ranging from 0.04 to 0.25. The total pore volume was determined from the amount of N_2 adsorbed at $P/P_0 = 0.975$. The diameter of mesopores was obtained from the pore size distribution calculated using the Barrett–Joyner–Halenda (BJH) equation applied to the desorption branch of the isotherm. As a result, the specific surface area of so-synthesized SBA-15 is 666 $m^2\ g^{-1}$ and the total pore volume is 1.25 $cm^3\ g^{-1}$. The pore size distribution is centered at 7.2 nm.

2.2 Preparation of Chlorophyll *a*-SBA-15 Conjugates

Chl *a* was either extracted from pea plants and purified according to Booth et al. [36], or purchased from Merck. The Chl *a*-SBA-15 conjugates were prepared by absorption of Chl *a* from solution: 400 µL of Chl *a* 140 µM in a 2-methyltetrahydrofuran (MeTHF) solution are added to 10 mg of SBA-15. The sample is then mixed and sonicated for 5 min to ensure the homogeneity of the suspension. The solvent is evaporated in open air, with the sample covered from direct light to protect the pigment. Once the solvent is evaporated, the sample is further dried in a vacuum

desiccator overnight. The sample is finally transferred to a quartz EPR tube with a diameter varying from 2 to 4 mm, and oxygen is removed by placing the sample in a vacuum line at a pressure of 10^{-4} mbar for 30 min before sealing.

2.3 Preparation of WSCP-SBA-15 Conjugates

Protein overexpression of *Lepidium virginicum* WSCP apoprotein in *Escherichia coli* and subsequent purification have been performed as previously reported [18]. The purified WSCP apoprotein was reconstituted with Chl *a* as previously described [37]. Two different solutions of WSCP have been prepared using buffers at different pH: 4.0 and 7.8. For the solution of WSCP at pH = 4.0 a citric acid-Na_2HPO_4 buffer was prepared. For the solution of WSCP at pH = 7.8 a phosphate buffer was prepared. Samples at the two pH values were prepared adding the appropriate buffer to two concentrated stock solutions of protein for a final volume of 1 mL of 3.6 µM solutions. WSCP-SBA-15 conjugates were prepared by addition of the 1 mL of WSCP solution to 10 mg of SBA-15. The suspensions were stirred for 4 h at 4°C. Subsequently, the samples were centrifuged three times for 5 min at 13,400 rpm. Between each centrifugation step, the supernatant is removed from the pellet and collected separately. The pellet is then recovered and dried overnight. Finally, the samples were transferred to quartz EPR tubes with diameter varying from 2 to 4 mm, and oxygen was removed by placing the samples in a vacuum line at a pressure of 10^{-4} mbar for 30 min.

2.4 UV–Vis Spectroscopy

UV-Vis experiments were performed on a dual beam spectrometer JASCO V-730ST, equipped with a deuterium lamp to record spectra from 190 to 370 nm and a tungsten halogen lamp to record spectra from 320 to 1100 nm. The reported spectra were recorded in the range 350–800 nm, with a data interval of 0.5 nm and a scan speed of 200 nm/min.

2.5 TR-EPR Experiments

TR-EPR experiments were performed at 80 K on a Bruker ELEXSYS E580, equipped with an ER 4118X-MD5 dielectric cavity, an Oxford CF935 liquid helium flow cryostat, and an Oxford ITC4 temperature controller. The microwave frequency was measured by a frequency counter, HP5342A. The temperature in the cryostat was controlled by a thermostated nitrogen-flow and all experiments were conducted at room temperature or at 80 K, disabling magnetic field modulation. Photo-excitation was conducted with a Nd:YAG pulsed laser (Quantel Brilliant) equipped with both second and third harmonic modules and an optical parametric oscillator (OPOTECH) (pulse length = 5 ns, E/pulse ≅ 2 mJ, 10 Hz repetition time). The EPR direct-detected signal, after preamplification with a 6 MHz amplifier, was recorded with a LeCroy 9300 digital oscilloscope, triggered by the laser pulse. At each magnetic field position, an average of about 300 transient signals was usually recorded; 256

points on the magnetic field axis were recorded, with a sweep width of 130.0 mT. The microwave power for TR-EPR experiments was set to be low enough (20–25 dB attenuation, i.e., 1.5 mW or less) to be in a low-power regime and avoid Torrey oscillations on the time trace. The time vs field surfaces were processed using a home-written MATLAB program that removes the background signal before the laser pulse (signal *vs* magnetic field) and the intrinsic response of the cavity to the laser pulse (signal vs time). The TR-EPR spectra shown in the main text were extracted from the surface at 1100 ns from the laser flash, about 100 ns after the maximum in the transient to avoid potential distortions. TR-EPR spectral simulations were performed with EasySpin version 6.0.0—dev.51. The ZFS parameters have been estimated directly from the spectra; the populations and relative amounts of the different spectral components have been obtained by automated fitting using a Levenberg–Marquardt algorithm within the EasySpin package (esfit function) [38].

3 Results and Discussion

3.1 Chl *a*-SBA-15

Chl *a* was incorporated into silica SBA-15 as described in the materials and methods. The conjugate was characterized by TR-EPR to verify whether the adsorption on the solid silica matrix alters the properties of the Chl *a* triplet state. Note that Chl *a* is easily desorbed from the Mesoporous Silica (MS) by soaking the loaded nanoparticles in MeTHF, the same solvent as the one used for the adsorption of Chl *a*, allowing to characterize the pigment after having been incorporated into the MS. Conversely, since Chl *a* is not soluble in water, adsorbed Chl *a* does not leach quantitatively from SBA-15 into an aqueous solution, justifying its potential applications.

We performed a TR-EPR analysis of Chl *a* in three different conditions: (i) dissolved in a MeTHF solution, (ii) adsorbed on SBA-15 (powder sample), (iii) Chl *a* extracted from SBA-15 using MeTHF. The TR-EPR spectra of Chl *a* (black lines) and the relative simulations (colored lines) are reported in Fig. 2 (top): (a) in MeTHF solution; (b) adsorbed on SBA-15 powder; (c) in MeTHF solution extracted from the MS. The triplet parameters are reported in Table 1. The UV-Vis spectra of Chl *a* are reported in Fig. 2 (bottom): Chl *a* in MeTHF—black; Chl *a* extracted from SBA-15 in MeTHF—blue; and for comparison pheophorbide *a* in MeTHF—green.

The TR-EPR spectra in the three samples are all different, however, their lineshapes are all compatible with population of the triplet state via Intersystem-Crossing (ISC). The triplet observed for the Chl *a*/SBA-15 conjugate (Fig. 2b) has larger $|D|$ and smaller $|E|$ than the triplet observed for Chl *a* in MeTHF solution (Fig. 2a): $D_{\text{Chl } a/\text{SBA-15}} = 0.0320\ \text{cm}^{-1}$ vs $D_{\text{Chl } a} = 0.0285\ \text{cm}^{-1}$. Note that the positive sign of D (and negative sign of E) has been chosen according to literature data on Chl *a* and is the norm for triplet states of prolate molecules [40]. The triplet signal observed after extraction of the pigment in MeTHF (Fig. 2c) shows the presence of two different species, with parameters that are compatible with those of the two triplets just described; the prevalent triplet is the one with the larger D value. The comparison of the fitted ZFS parameters of the two species with literature data on porphyrin triplet

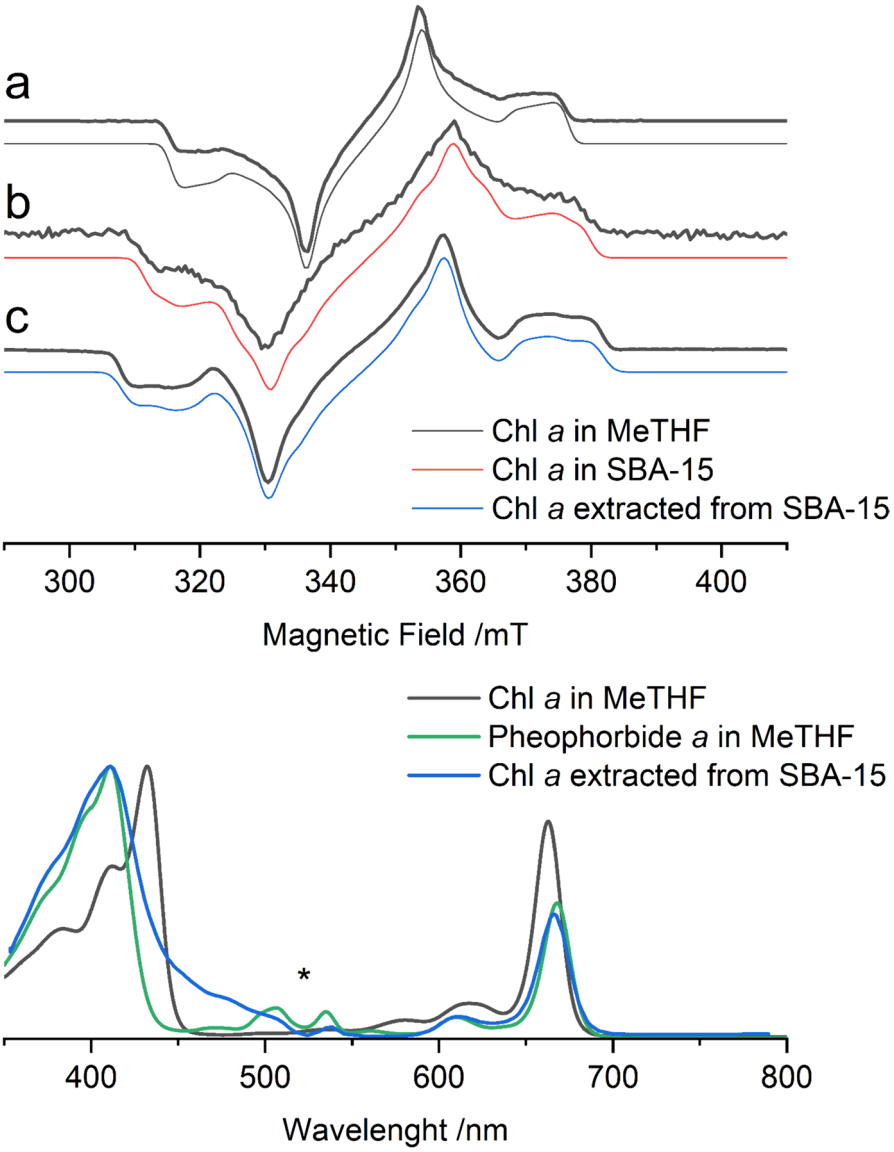

Fig. 2 Top. TR-EPR spectra (black) and simulations (color) of Chl *a*: **a** MeTHF frozen solution—black; **b** adsorbed on SBA-15 powder—red; **c** MeTHF frozen solution extracted from the MS—blue. All spectra are recorded at 80 K with laser excitation at 532 nm and are normalized to unit intensity. Bottom. UV-Vis spectra of Chl *a*: Chl *a* in MeTHF – black; Chl *a* extracted from SBA-15 in MeTHF—blue; pheophorbide *a* in MeTHF—green. All spectra have been normalized to unit intensity for better comparison. The asterisk denotes the region of the absorption peaks typical of the de-metalated Chl *a* ring

states [39], allows us to establish that the main species is pheophytin *a*, i.e., Chl *a* without the central Mg^{2+} ion, while the minor species is Chl *a*. The presence of pheophytin is further confirmed from the comparison of the UV-Vis spectrum of the

Table 1 Triplet state parameters of Chl *a* in the different samples discussed in this work

Sample	$D/10^{-4}$ cm^{-1}	$E/10^{-4}$ cm^{-1}	p_x:p_y:p_z	%
MeTHF	285	− 40	0.28:0.72:0.00	100
SBA-15	285	− 40	0.43:0.57:0.00	25
	320	− 20	0.43:0.57:0.00	75
SBA-15 extract	285	− 40	0.28:0.72:0.00	18
	345	− 30	0.28:0.72:0.00	82
SBA-15OH	284	− 36	0.43:0.57:0.00	100
SBA-15OH extract	285	− 42	0.34:0.66:0.00	100
WSCP	288	− 36	0.26:0.74:0.00	100
WSCP in SBA-15 pH 4.0	288	− 36	0.35:0.65:0.00	75
	320	− 20	0.43:0.57:0.00	25
WSCP in SBA-15 pH 7.8	288	− 36	0.35:0.65:0.00	35
	320	− 20	0.43:0.57:0.00	65

All parameters have been obtained by fitting the TR-EPR spectra using EasySpin. The simulations were performed assuming a positive sign of *D* and a negative sign of *E* according to literature data on Chl *a* [39]. The last column reports the % of each triplet spectral component present; when two components are present the one with larger *D* is reported last. Uncertainties are $\pm 5 \cdot 10^{-4}$ cm^{-1} for ZFS parameters and ± 0.01 for triplet sublevel populations as estimated from the variability of the spectral fitting

extracted pigments with the spectrum of the stock solution of chlorophyll in MeTHF and of pheophorbide *a* (i.e., pheophytin *a* analog without the long phytyl chain). Note that the spectrum of the extract shows some scattering by the residual matrix suspended in solution. The two peaks at 506 nm and 536 nm, indicated by the asterisk in Fig. 2 (bottom), are typical of pheophytin [41], as is the maximum of the Soret band at 411 nm. Furthermore, the Q_y (S_1) band of the extract is at 666 nm, while the reference has the Q_y band at 663 nm. The presence of small amounts of pristine Chl *a*, as indicated by the TR-EPR spectrum, is here proven by the presence of a shoulder of the Soret band (around 430 nm).

A second difference between the samples is related to the triplet sublevel populations, with a redistribution of the populations between T_y and T_x sublevels upon inclusion of the pigment in SBA-15. Upon extraction of the pigment, the triplet sublevel populations return to the same pattern observed for Chl *a* in frozen solution, for both triplet species. Since the populations are strongly related to the environment, the presence of such a difference, being removed upon extraction, is a confirmation that the triplet state observed in Fig. 2b is relative to the Chl *a* molecules included in the solid matrix. Note that the change in the spin polarization of the TR-EPR spectra can give information on the ISC process, and thus on the symmetry of the states involved; a full interpretation requires however a computational effort beyond the scope of this work.

The combination of the TR-EPR and UV-Vis data show that the incorporation of Chl *a* inside the SBA-15 matrix leads, at least at some extent, to loss of the central Mg^{2+} ion. The de-metalation of Chl *a* is reported to take place in acidic conditions, as a consequence of the protonation of the nitrogen atoms of the pyrrole rings, and we suggest that this happens because of the SBA-15 properties. SBA-15 contains

two types of surface silanol groups: isolated silanols with pKa about 2 and geminal silanols with pKa about 8.2, but four less times abundant that the isolated ones [42]; it is expected that, after rinsing SBA-15 with water (pH about 5) as a final step of its synthesis procedure, only 20% of the surface silanol groups are deprotonated. This was also confirmed by the measurement of a slightly negative zeta potential of the material at this pH [43]. Therefore, SBA-15 is likely able to exchange the Mg^{2+} ion with protons, thus leading to pheophytin formation.

Pheophytin is able to produce singlet oxygen even at higher yields than Chl *a* [44, 45], thus this sample is likely useful for $^1O_2$ production. However, further effort must be devoted to preparing a sample that preserves the pigment in its pristine state.

3.2 Chl *a*/Base-Treated SBA-15

In light of the de-metalation of Chl *a* in as-prepared SBA-15, we attempted to deprotonate the acidic silanolic groups by washing the MS powder with a basic solution of NaOH in ethanol (0.17% w/v). The base-treated SBA-15 (in short, SBA-15OH) powder was then dried under vacuum. Chl *a* was adsorbed on SBA-15OH as described in the materials and methods, and the conjugate was characterized by TR-EPR.

We performed a TR-EPR analysis of Chl *a* adsorbed on SBA-15OH (powder sample), and then on a frozen solution of Chl *a* extracted from SBA-15OH using MeTHF. The TR-EPR spectra of Chl *a* are reported in Fig. 3 (top): (a) MeTHF solution; (b) adsorbed on SBA-15OH powder; (c) in MeTHF solution extracted from the MS. The triplet parameters are reported in Table 1. The UV-Vis spectra of Chl *a* are reported in Fig. 3 (bottom): Chl *a* in MeTHF—black; Chl *a* extracted from SBA-15OH in MeTHF—blue.

The TR-EPR spectra in the solid matrix and following the extraction in MeTHF are similar, showing a triplet state with very close ZFS parameters, but different polarization patterns. The ZFS parameters obtained from spectral fitting after the extraction from the solid matrix, $|D|=0.0285$ cm^{-1} and $|E|=0.0042$ cm^{-1}, agree with those of Chl *a* triplet state in MeTHF. The polarization changes are reflected in the triplet sublevel populations reported in Table 1. The changes in polarization are analogous to those observed above for native SBA-15, once again confirming the inclusion of the pigment in the MS. The change in polarization reverts once the pigment is extracted except for a slight difference probably due to some residual EtOH/NaOH solution inside the MS extracted together with Chl *a* and thus the solution of the extract is not identical to the initial one.

The UV-Vis spectrum of the pigment in MeTHF extracted from the sample (Fig. 3b) further confirms that Chl *a* is only minimally altered in this preparation. Comparison to the spectrum of the stock solution (Fig. 2a) shows that both spectra have identical Soret bands (note that the spectrum of the extract shows some scattering by the residual matrix suspended in solution), while the maximum of the Q_y band shifts from 663 nm in the MeTHF stock to 664 nm in the extract. Also, in stark contrast to the sample extracted from untreated SBA-15, there are no peaks at 506 nm and 536 nm confirming the absence of pheophytin in these samples.

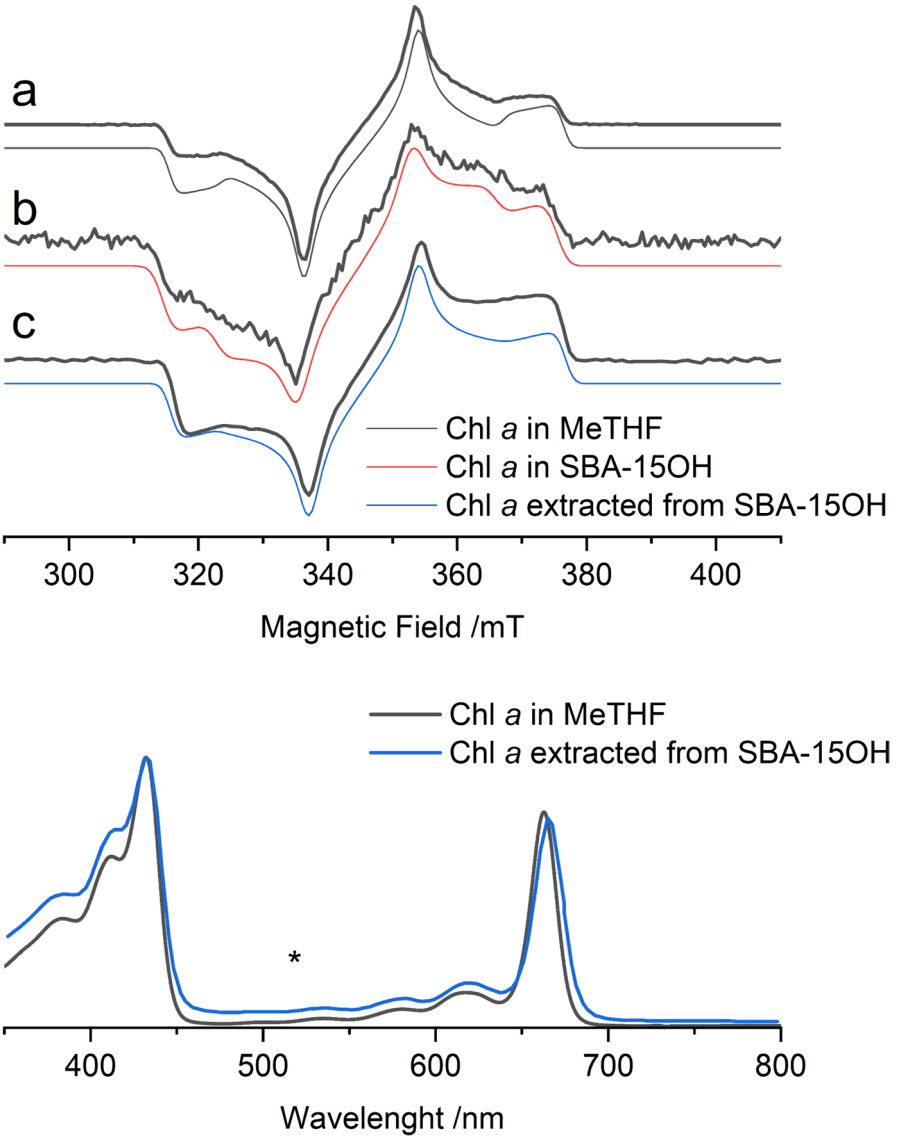

Fig. 3 Top. TR-EPR spectra (black) and simulations (color) of Chl *a*: **a** MeTHF frozen solution—black; **b** adsorbed on SBA-15OH powder—red; **c** MeTHF frozen solution extracted from the MS—blue. All spectra are recorded at 80 K with laser excitation at 532 nm and are normalized to unit intensity. Bottom. UV-Vis spectra of Chl *a*: Chl *a* in MeTHF—black; Chl *a* extracted from SBA-15 in MeTHF—blue. All spectra have been normalized to unit intensity for better comparison. The asterisk denotes the region of the absorption peaks typical of the de-metalated Chl *a* ring

Summing up the results, we can confirm that the neutralization treatment on the MS is efficient in preventing Chl *a* de-metalation thus preserving the pigment characteristics.

3.3 WSCP/SBA-15

The adsorption of proteins inside MS is dependent on the pH of the matrix relatively to the isoelectric point (IP) of the protein: a net positive charge of the protein will favor the interaction with a silica support that has a negative charge on its surface [46]. Then, in the preparation of the WSCP/SBA-15 conjugate special attention should be devoted to the pH of the buffer. To promote WSCP adsorption, solutions should be prepared with a pH = 4 or lower ($IP_{WSCP} \approx 4.2–4.5$ [47]). Note that WSCP is especially robust and, even though pH = 4 is far below the pH at which WSCP is normally isolated (pH = 7.8), the UV-Vis and circular dichroism spectra show no signs of denaturation [22]. Nevertheless, we explored the pH dependence of the samples by preparing the WSCP/SBA-15 conjugate by performing the adsorption step in an acidic buffer (pH = 4) or in the buffer in which WSCP is purified (pH = 7.8).

The two SBA-15 samples behaved very differently from the point of view of WSCP incorporation. As expected, the sample at pH = 4 quantitatively adsorbs WSCP, as shown by visible solution discoloration. We used UV-Vis to monitor the solution: after 4 h in presence of SBA-15, only 20% of the initial WSCP was remaining in the supernatant, estimated from the Q_y band maximum at 664 nm (± 10%, due to the scattering from residual matrix particles, data not shown). Conversely, for the sample at pH = 7.8, the solution remains colored: WSCP in the supernatant following SBA-15 addition decreases by only 35%, estimated from the Q_y band (± 10%, due to the scattering from residual matrix particles, data not shown). The UV-Vis spectrum of WSCP at pH = 7.8 is shown in Fig. 4 (bottom).

The TR-EPR spectra of WSCP in the different samples are reported in Fig. 4 (top): (a) WSCP in buffer at pH = 7.8; (b) WSCP adsorbed on SBA-15 powder prepared starting from pH = 4; (c) WSCP adsorbed on SBA-15 powder prepared starting from pH = 7.8. The triplet states parameters of WSCP in buffer are reported in Table 1 and are identical to those previously reported [48]. Interestingly, both conjugates show TR-EPR spectra with multiple triplet species: one species is a triplet almost identical to the one observed for WSCP in buffered frozen solution, while the second species has larger D and slightly lower E. The amount of two triplet species depends on the starting pH: the spectrum of the sample prepared starting from the buffer at pH = 7.8 is dominated by the second species, while the opposite is true for the one prepared starting from pH = 4. The species with larger D has ZFS parameters similar to those previously discussed and assigned to the pheophytin triplet state. Note that given the high affinity of WSCP for the MS, it is not feasible to quantitatively extract the protein from the MS and, therefore, we could not characterize the released protein solution as previously performed for Chl *a*.

The TR-EPR spectra suggest that the Chl *a* bound to WSCP that is immobilized on SBA-15 either remains unaltered or is transformed into pheophytin. In the latter case, as leaching of Chl *a* and subsequent loss of Mg^{2+} is unlikely to occur in natively-folded WSCP due to the high stability of the pigment [22], a suitable explanation of this effect is that WSCP undergoes partial deformation or denaturation to fit inside the pores. The average pore diameter of SBA-15 is 7 nm, whereas the hydrodynamic radius of WSCP is slightly less than 7 nm. We hypothesize that the deformation leads either to a larger exposition of the pigment or directly to Chl *a*

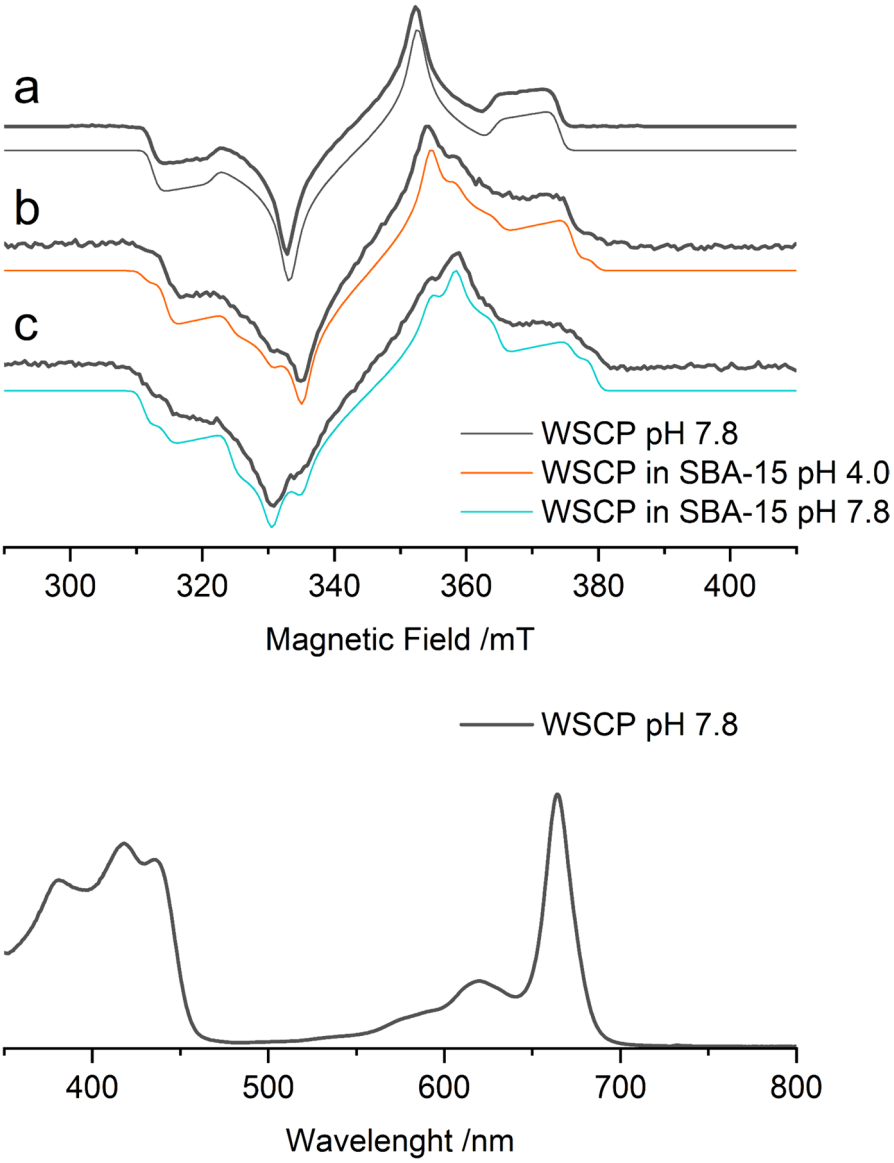

Fig. 4 Top. TR-EPR spectra (black) and simulations (color) of WSCP: **a** buffer (pH = 7.8) and glycerol frozen solution—black; **b** adsorbed on SBA-15 powder starting from pH = 4—orange; **c** adsorbed on SBA-15 powder starting from pH = 7.8—azure. All spectra are recorded at 80 K with laser excitation at 532 nm and are normalized to unit intensity. Bottom. UV-Vis spectrum of WSCP in buffer at pH = 7.8

leaching, thus exposing the Mg^{2+} to proton exchange. This process is however not fully understood and is still under investigation.

Overall, the inclusion of WSCP in SBA-15 was successful, but the changes in the triplet state parameters suggest that the protein structure is not fully preserved

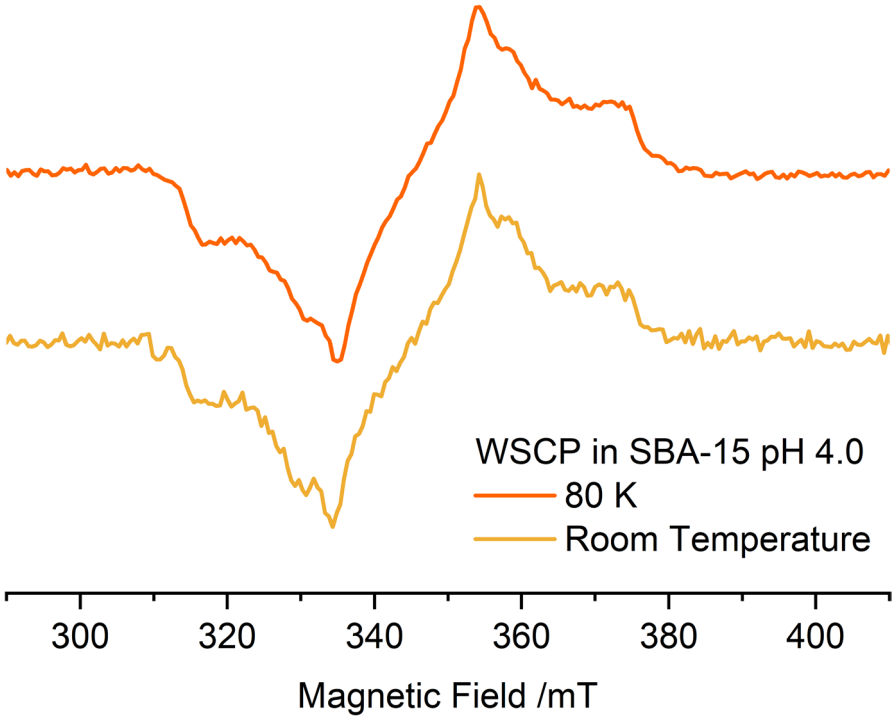

Fig. 5 TR-EPR spectra of WSCP adsorbed on SBA-15 powder starting from pH = 4. **a** 80 K—orange; **b** room temperature—yellow. All spectra are recorded with laser excitation at 532 nm and are normalized to unit intensity

exposing the pigment inside the protein. As a consequence, Chl *a* is altered and loses its stability compared to the protein in solution.

3.4 Experiments at Room Temperature

We also performed TR-EPR experiments at room temperature on WSCP in SBA-15. The samples show the presence of the same triplet states observed at 80 K, usually with worse *S*/*N* ratio. A selected spectrum is reported in Fig. 5 (yellow), together with its counterpart at 80 K (orange). The spectrum at room temperature does not show any averaging of the ZFS parameters, suggesting that the pigments are immobilized inside the protein-MS system.

4 Conclusion

Materials containing either chlorophyll *a* or WSCP embedded in the pores of Mesoporous Silica Nanoparticles SBA-15 have been characterized via TR-EPR, the technique of choice given the importance of the paramagnetic triplet state of Chl *a*.

Despite this technique was never used before in these kinds of samples to assess the loading of the molecules into the matrix, it proved to be relevant for monitoring the change of the polarization of the triplet state. Indeed, the parameters of the triplet state change not only when the pigment is altered (in this case loss of the central ion) but also between frozen solution and inside the MS, an information not easily accessible otherwise. The experiments showed that, depending on the protonation state of SBA-15, Chl *a* is incorporated either as pristine pigment or as pheophytin *a*. In the case of WSCP, the inclusion of the protein in the MS is quantitative at pH 4 but causes an alteration of the pigment. The loss of the central metal in WSCP implies that the inclusion in SBA-15 leads to a partial deformation/denaturation of WSCP with consequent loss of its shielding effect on Chl *a*.

We showed that the triplet state of Chl *a* in the solid matrix is detectable even at room temperature, suggesting that the matrix efficiently immobilizes it, and it is very sensitive to the chemical state of Chl *a* in these samples.

In the future, the current samples will be tested for singlet oxygen production and tested for a potential photoprotective effect of the MS using fluorescence and EPR. Overall, while SBA-15 proved a good MS for the production of solid samples to be tested for PDT, to fully harness the potentiality of the protein/MS conjugate a different MS, likely with larger pores, is needed.

Acknowledgements A.A. is very grateful to Harald Paulsen and Daniel M. Palm (Johannes Gutenberg University Mainz) for their support in the preparation of the WSCP samples.

Author Contributions Conceptualization: D.C., A.M., M.B.; Methodology: all authors; Formal analysis and investigation: S.Z., M.B; Writing—original draft preparation: S.Z., D.C., M.B.; Writing—review and editing: M.B.; Resources: D.C.; Supervision: D.C.. All authors reviewed the manuscript.

Funding Open access funding provided by Università degli Studi di Padova within the CRUI-CARE Agreement. M.B. acknowledges the financial support of University of Padova (P-DiSC#02BIRD2020-UNIPD).

Availability of Data and Materials Data are available upon request to the corresponding author.

Declarations

Conflict of Interest The authors declare no competing financial and/or non-financial interests.

Ethical Approval Not applicable.

References

1. A.V. Kustov, D.V. Belykh, N.L. Smirnova, E.A. Venediktov, T.V. Kudayarova, S.O. Kruchin, I.S. Khudyaeva, D.B. Berezin, Synthesis and investigation of water-soluble chlorophyll pigments for antimicrobial photodynamic therapy. Dye. Pigment. **149**, 553–559 (2018). https://doi.org/10.1016/j.dyepig.2017.09.073
2. Y.-H. Gao, X.-X. Zhu, W. Zhu, D. Wu, D.-Y. Chen, Y.-J. Yan, X.-F. Wu, D.F. O'Shea, Z.-L. Chen, Synthesis and evaluation of novel chlorophyll a derivatives as potent photosensitizers for photodynamic therapy. Eur. J. Med. Chem. **187**, 111959 (2020). https://doi.org/10.1016/j.ejmech.2019.111959
3. Y. Feng, H. Cheng, J. Han, X. Zheng, Y. Liu, Y. Yang, L. Zhang, Chlorophyll sensitized BiVO 4 as photoanode for solar water splitting and CO2 conversion. Chin. Chem. Lett. **28**, 2254–2258 (2017). https://doi.org/10.1016/j.cclet.2017.10.025
4. K. Roy, D. Ghosh, K. Sarkar, P. Devi, P. Kumar, Chlorophyll(*a*)/carbon quantum dot bio-nanocomposite activated nano-structured silicon as an efficient photocathode for photoelectrochemical water splitting. ACS Appl. Mater. Interfaces **12**, 37218–37226 (2020). https://doi.org/10.1021/acsami.0c10279
5. M. Mohsin, T. Ishaq, I.A. Bhatti, M. Maryam, A. Jilani, A.A. Melaibari, N.H. Abu-Hamdeh, Semiconductor nanomaterial photocatalysts for water-splitting hydrogen production: the holy grail of converting solar energy to fuel. Nanomaterials **13**, 546 (2023). https://doi.org/10.3390/nano13030546
6. E. Nikoloudakis, I. López-Duarte, G. Charalambidis, K. Ladomenou, M. Ince, A.G. Coutsolelos, Porphyrins and phthalocyanines as biomimetic tools for photocatalytic H2 production and CO2 reduction. Chem. Soc. Rev. **51**, 6965–7045 (2022). https://doi.org/10.1039/D2CS00183G
7. N. Himeshima, Y. Amao, Photoinduced hydrogen production from cellulose derivative with chlorophyll-*a* and platinum nanoparticles system. Energy Fuels **17**, 1641–1644 (2003). https://doi.org/10.1021/ef034006w
8. A. Kay, M. Graetzel, Artificial photosynthesis. 1. Photosensitization of titania solar cells with chlorophyll derivatives and related natural porphyrins. J. Phys. Chem. **97**, 6272–6277 (1993). https://doi.org/10.1021/j100125a029
9. Y. Amao, Y. Maki, Y. Fuchino, Photoinduced hydrogen production with artificial photosynthesis system based on carotenoid−chlorophyll conjugated micelles. J. Phys. Chem. C **113**, 16811–16815 (2009). https://doi.org/10.1021/jp900063r
10. P.G. Bowers, G. Porter, Quantum yields of triplet formation in solutions of chlorophyll. Proc. R. Soc. Lond. A Math. Phys. Sci. **296**, 435–441 (1967)
11. H. Küpper, R. Dědic, A. Svoboda, J. Hála, P.M. Kroneck, Kinetics and efficiency of excitation energy transfer from chlorophylls, their heavy metal-substituted derivatives, and pheophytins to singlet oxygen. Biochim. Biophys. Acta Gen. Subj. **1572**, 107–113 (2002). https://doi.org/10.1016/S0304-4165(02)00284-2
12. A.A. Krasnovsky, Y.V. Kovalev, Spectral and kinetic parameters of phosphorescence of triplet chlorophyll *a* in the photosynthetic apparatus of plants. Biochemistry **79**, 349–361 (2014). https://doi.org/10.1134/S000629791404004X
13. C.H. Foyer, J. Harbinson, Relationships between antioxidant metabolism and carotenoids in the regulation of photosynthesis, in *The photochemistry of carotenoids*. (Kluwer Academic Publishers, Dordrecht, 2004), pp.305–325
14. D. Siefermann-Harms, The light-harvesting and protective functions of carotenoids in photosynthetic membranes. Physiol. Plant. **69**, 561–568 (1987). https://doi.org/10.1111/j.1399-3054.1987.tb09240.x
15. G.F. Peter, J.P. Thornber, Biochemical composition and organization of higher plant photosystem II light-harvesting pigment-proteins. J. Biol. Chem. **266**, 16745–16754 (1991)
16. D. Horigome, H. Satoh, N. Itoh, K. Mitsunaga, I. Oonishi, A. Nakagawa, A. Uchida, Structural mechanism and photoprotective function of water-soluble chlorophyll-binding protein. J. Biol. Chem. **282**, 6525–6531 (2007). https://doi.org/10.1074/jbc.M609458200
17. A. Agostini, D.M. Palm, H. Paulsen, D. Carbonera, Accessibility of protein-bound chlorophylls probed by dynamic electron polarization. J. Phys. Chem. Lett. **9**, 672–676 (2018)

18. A. Agostini, D.M. Palm, F.-J. Schmitt, M. Albertini, M. Di Valentin, H. Paulsen, D. Carbonera, An unusual role for the phytyl chains in the photoprotection of the chlorophylls bound to water-soluble chlorophyll-binding proteins. Sci. Rep. **7**, 7504 (2017). https://doi.org/10.1038/s41598-017-07874-6
19. N. Dodge, D.A. Russo, B.M. Blossom, R.K. Singh, B. van Oort, R. Croce, M.J. Bjerrum, P.E. Jensen, Water-soluble chlorophyll-binding proteins from brassica oleracea allow for stable photobiocatalytic oxidation of cellulose by a lytic polysaccharide monooxygenase. Res. Sq. (2020). https://doi.org/10.21203/rs.3.rs-40886/v1
20. D.M. Palm, A. Agostini, A.-C. Pohland, M. Werwie, E. Jaenicke, H. Paulsen, Stability of water-soluble chlorophyll protein (WSCP) depends on phytyl conformation. ACS Omega **4**, 7971–7979 (2019). https://doi.org/10.1021/acsomega.9b00054
21. K. Schmidt, C. Fufezan, A. Krieger-Liszkay, H. Satoh, H. Paulsen, Recombinant water-soluble chlorophyll protein from brassica oleracea var botrys binds various chlorophyll derivatives. Biochemistry **42**, 7427–7433 (2003). https://doi.org/10.1021/bi034207r
22. D.M. Palm, A. Agostini, S. Tenzer, B.M. Gloeckle, M. Werwie, D. Carbonera, H. Paulsen, Water-soluble chlorophyll protein (WSCP) stably binds two or four chlorophylls. Biochemistry **56**, 1726–1736 (2017). https://doi.org/10.1021/acs.biochem.7b00075
23. O. Hocine, M. Gary-Bobo, D. Brevet, M. Maynadier, S. Fontanel, L. Raehm, S. Richeter, B. Loock, P. Couleaud, C. Frochot, Silicalites and mesoporous silica nanoparticles for photodynamic therapy. Int. J. Pharm. **402**, 221–230 (2010). https://doi.org/10.1016/j.ijpharm.2010.10.004
24. M. Gary-Bobo, O. Hocine, D. Brevet, M. Maynadier, L. Raehm, S. Richeter, V. Charasson, B. Loock, A. Morère, P. Maillard et al., Cancer therapy improvement with mesoporous silica nanoparticles combining targeting, drug delivery and PDT. Int. J. Pharm. **423**, 509–515 (2012). https://doi.org/10.1016/j.ijpharm.2011.11.045
25. G.J. Owens, R.K. Singh, F. Foroutan, M. Alqaysi, C.-M. Han, C. Mahapatra, H.-W. Kim, J.C. Knowles, Sol-gel based materials for biomedical applications. Prog. Mater. Sci. **77**, 1–79 (2016). https://doi.org/10.1016/j.pmatsci.2015.12.001
26. T. Itoh, K. Yano, Y. Inada, Y. Fukushima, Stabilization of chlorophyll *a* in mesoporous silica and its pore size dependence. J. Mater. Chem. **12**, 3275–3277 (2002). https://doi.org/10.1039/B203923K
27. T. Itoh, K. Yano, Y. Inada, Y. Fukushima, Photostabilized chlorophyll *a* in mesoporous silica: adsorption properties and photoreduction activity of chlorophyll *a*. J. Am. Chem. Soc. **124**, 13437–13441 (2002). https://doi.org/10.1021/ja0203059
28. V. Rizzi, J. Gubitosa, P. Fini, F. Fanelli, A. Fraix, S. Sortino, A. Agostiano, L. De Cola, A. Nacci, P. Cosma, A comprehensive investigation of amino grafted mesoporous silica nanoparticles supramolecular assemblies to host photoactive chlorophyll *a* in aqueous solution. J. Photochem. Photobiol. A Chem. **377**, 149–158 (2019). https://doi.org/10.1016/j.jphotochem.2019.03.041
29. D. Zhao, J. Feng, Q. Huo, N. Melosh, G.H. Fredrickson, B.F. Chmelka, G.D. Stucky, Triblock copolymer syntheses of mesoporous silica with periodic 50–300 angstrom pores. Science **279**, 548–552 (1998). https://doi.org/10.1126/science.279.5350.548
30. S. Jafari, H. Derakhshankhah, L. Alaei, A. Fattahi, B.S. Varnamkhasti, A.A. Saboury, Mesoporous silica nanoparticles for therapeutic/diagnostic applications. Biomed. Pharmacother. **109**, 1100–1111 (2019). https://doi.org/10.1016/j.biopha.2018.10.167
31. W. Li, Q. Yue, Y. Deng, D. Zhao, Ordered Mesoporous Materials Based on Interfacial Assembly and Engineering. Adv. Mater. **25**, 5129–5152 (2013). https://doi.org/10.1002/adma.201302184
32. Z. Li, Y. Zhang, N. Feng, Mesoporous silica nanoparticles: synthesis, classification, drug loading, pharmacokinetics, biocompatibility, and application in drug delivery. Expert Opin. Drug Deliv. **16**, 219–237 (2019). https://doi.org/10.1080/17425247.2019.1575806
33. I.N. Serratos, F. Rojas-González, R. Sosa-Fonseca, J.M. Esparza-Schulz, V. Campos-Peña, S.R. Tello-Solís, M.A. García-Sánchez, Fluorescence optimization of chlorophyll covalently bonded to mesoporous silica synthesized by the sol–gel method. J. Photochem. Photobiol. A Chem. **272**, 28–40 (2013). https://doi.org/10.1016/j.jphotochem.2013.08.014
34. M. García-Sánchez, I. Serratos, R. Sosa, T. Tapia-Esquivel, F. González-García, F. Rojas-González, S. Tello-Solís, A. Palacios-Enriquez, J. Esparza Schulz, A. Arrieta, Chlorophyll *a* covalently bonded to organo-modified translucent silica xerogels: optimizing fluorescence and maximum loading. Molecules **21**, 961 (2016). https://doi.org/10.3390/molecules21070961
35. I.N. Serratos, H.J. Avila-Paredes, I. Hernández-Reséndiz, A. Santamaría, V. Bustos-Terrones, P. Ruiz Sánchez, G. Saucedo-Castañeda, J.M. Esparza Shulz, A. Arrieta, R. Sosa, Entrapment of chlorophyll from chlorella vulgaris and chlorella protothecoides into microporous silica synthesized by a sol–gel method. J. Phys. Commun. **5**, 105004 (2021). https://doi.org/10.1088/2399-6528/ac26df

36. P.J. Booth, H. Paulsen, Assembly of light-harvesting chlorophyll *a/b* complex in vitro time-resolved fluorescence measurements. Biochemistry **35**, 5103–5108 (1996). https://doi.org/10.1021/bi953053f
37. D.M. Palm, A. Agostini, V. Averesch, P. Girr, M. Werwie, S. Takahashi, H. Satoh, E. Jaenicke, H. Paulsen, Chlorophyll *a/b* binding-specificity in water-soluble chlorophyll protein. Nat. Plants **4**, 920–929 (2018). https://doi.org/10.1038/s41477-018-0273-z
38. S. Stoll, A. Schweiger, EasySpin, a comprehensive software package for spectral simulation and analysis in EPR. J. Magn. Reson. **178**, 42–55 (2006). https://doi.org/10.1016/j.jmr.2005.08.013
39. R.H. Clarke, R.E. Connors, T.J. Schaafsma, J.F. Kleibeuker, R.J. Platenkamp, The triplet state of chlorophylls. J. Am. Chem. Soc. **98**, 3674–3677 (1976). https://doi.org/10.1021/ja00428a048
40. S. Richert, C.E. Tait, C.R. Timmel, Delocalisation of photoexcited triplet states probed by transient EPR and hyperfine spectroscopy. J. Magn. Reson. **280**, 103–116 (2017). https://doi.org/10.1016/j.jmr.2017.01.005
41. A.E. Sommer Márquez, D.A. Lerner, G. Fetter, P. Bosch, D. Tichit, E. Palomares, Preparation of layered double hydroxide/chlorophyll *a* hybrid nano-antennae: a key step. Dalt. Trans. **43**, 10521–10528 (2014). https://doi.org/10.1039/C4DT00113C
42. J.M. Rosenholm, T. Czuryszkiewicz, F. Kleitz, J.B. Rosenholm, M. Lindén, On the Nature of the brønsted acidic groups on native and functionalized mesoporous siliceous SBA-15 as studied by benzylamine adsorption from solution. Langmuir **23**, 4315–4323 (2007). https://doi.org/10.1021/la062450w
43. S. Leccese, T. Onfroy, A. Wilson, D. Kirilovsky, S. Casale, S. Guira, M. Selmane, C. Jolivalt, A. Mezzetti, Immobilization of orange carotenoid protein on mesoporous silica SBA-15 for the development of photoactivable nanodevices. Microporous Mesoporous Mater. **340**, 112007 (2022). https://doi.org/10.1016/j.micromeso.2022.112007
44. A.A. Krasnovsky, K.V. Neverov, S.Y. Egorov, B. Roeder, T. Levald, Photophysical studies of pheophorbide a and pheophytin a. Phosphorescence and photosensitized singlet oxygen luminescence. J. Photochem. Photobiol. B Biol. **5**, 245–254 (1990). https://doi.org/10.1016/1011-1344(90)80009-M
45. M. Kotkowiak, A. Dudkowiak, L. Fiedor, Intrinsic photoprotective mechanisms in chlorophylls. Angew. Chemie Int. Ed. **56**, 10457–10461 (2017). https://doi.org/10.1002/anie.201705357
46. S. Hudson, J. Cooney, E. Magner, Proteins in mesoporous silicates. Angew. Chemie Int. Ed. **47**, 8582–8594 (2008). https://doi.org/10.1002/anie.200705238
47. T. Murata, C. Ishikawa, Chemical, physicochemical and spectrophotometric properties of crystalline chlorophyll-protein complexes from *Lepidium virginicum* L. Biochim. Biophys. Acta Bioenerg. **635**, 341–347 (1981). https://doi.org/10.1016/0005-2728(81)90032-3
48. S. Ciuti, A. Agostini, A. Barbon, M. Bortolus, H. Paulsen, M. Di Valentin, D. Carbonera, Magnetophotoselection in the investigation of excitonically coupled chromophores: the case of the water-soluble chlorophyll protein. Molecules **27**, 3654 (2022). https://doi.org/10.3390/molecules27123654